ACADEMIC PRESS

Available online at www.sciencedirect.com
SCIENCE DIRECT®

Journal of Catalysis 217 (2003) 69–78

JOURNAL OF CATALYSIS

www.elsevier.com/locate/jcat

# Effects of acidic and basic hydrolysis catalysts on the photocatalytic activity and microstructures of bimodal mesoporous titania

Jiaguo Yu,[a,b] Jimmy C. Yu,[b,*] Mitch K.-P. Leung,[b] Wingkei Ho,[b] Bei Cheng,[a] Xiujian Zhao,[a] and Jincai Zhao [c]

[a] *State Key Laboratory of Advanced Technology for Materials Synthesis and Processing, Wuhan University of Technology, Wuhan 430070, China*
[b] *Department of Chemistry, The Chinese University of Hong Kong, Shatin, New Territories, Hong Kong, China*
[c] *Laboratory of Photochemistry, Center for Molecular Science, Institute of Chemistry, The Chinese Academy of Science, Beijing 100080, China*

Received 14 August 2002; revised 13 January 2003; accepted 16 January 2003

**Abstract**

Bimodal mesoporous titania powders with high photocatalytic activity were prepared by hydrolysis of titanium tetraisopropoxide in the presence of $HNO_3$ or $NH_4OH$ under ultrasonic irradiation. The powders were characterized by X-ray diffraction (XRD), scanning electron microscopy (SEM), BET surface areas, and X-ray photoelectron spectroscopy (XPS). Photocatalytic activity was evaluated by the photocatalytic oxidation of acetone in air. The effects of catalysts added during hydrolysis on the microstructure and photocatalytic activity of the $TiO_2$ powders were investigated. The results showed that $HNO_3$ enhanced the growth of brookite, while $NH_4OH$ not only retarded phase transformation of the $TiO_2$ powders from amorphous to anatase and anatase to rutile but also suppressed the growth of brookite. All $TiO_2$ powders calcined from 400 to 600 °C showed bimodal pore-size distributions in the mesoporous region: one was intraaggregated pores with maximum pore diameters of ca. 4–9 nm and the other interaggregated ones with maximum pore diameters of ca. 35–50 nm. At 700 °C, the pore-size distributions of all samples exhibited monomodal distribution of the interaggregated pores due to the collapse of the intraaggregated pores. The photocatalytic activity of the $TiO_2$ powders prepared by this method and calcined at 400 °C exceeded that of Degussa P-25 when the molar ratio of $HNO_3$ or $NH_4OH$ to $H_2O$ was less than 0.05.


*Keywords:* Mesoporous titania; Titanium isopropoxide; Hydrolysis; $HNO_3$; $NH_4OH$; Microstructures; Photocatalytic activity

## 1. Introduction

A great deal of effort has been devoted in recent years to developing oxide semiconductor photocatalysts with high activities for environmental protection procedures such as air purification, water disinfection, hazardous waste remediation, and water purification [1–6]. Among various oxide semiconductor photocatalysts, titania has proven to be the most suitable for widespread environmental applications due to its biological and chemical inertness, strong oxidizing power, cost effectiveness, and long-term stability against photocorrosion and chemical corrosion. Titania has three different crystalline phases: rutile, anatase, and brookite, rutile among which is the thermodynamically stable state, while the other two phases are metastable [7]. Photocatalytic activity of titania is strongly dependent on its phase structure, crystallite size, specific surface areas, and pore structure [8–10]. For example, many studies have confirmed that the anatase phase of titania is a superior photocatalytic material attributable to the low recombination rate of its photogenerated electrons and holes [1,2]. Moreover, we found that the composite of two phases of titania was more beneficial for suppressing the recombination of photogenerated electrons and holes and thus enhanced photocatalytic activity [8,9]. However, the detailed mechanism and factors influencing its activity were poorly understood [11,12].

Sol–gel processing can be used to make nanometer-sized photocatalysts by a chemical reaction in solution starting with metal alkoxides as a precursor at room temperature [13,14]. An advantage of this method is that it is possible to obtain a large amount of $TiO_2$ powders with high photocatalytic activity and chemical purity [8,9,15]. In sol–gel synthesis of titania, hydrolysis and polycondensa-

* Corresponding author.
*E-mail address:* jimyu@cuhk.edu.hk (J.C. Yu).

0021-9517/03/$ – see front matter 
doi:10.1016/S0021-9517(03)00034-4

Table 1
Effects of amount of $HNO_3$ and $NH_4OH$ catalysts on relative crystallinity of anatase and pore volumes in $TiO_2$ xerogels dried at 100 °C

| Sample | Type of catalyst | Catalyst/TTIP molar ratio | pH | Relative crystallinity | BET surface area ($m^2/g$) | Pore volume ($cm^3/g$) |
|---|---|---|---|---|---|---|
| CAT1 | $HNO_3$ | 0.30 | 0.5 | 2.5 | 240.3 | 0.19 |
| CAT2 | $HNO_3$ | 0.05 | 4.1 | 2.3 | 246.1 | 0.29 |
| CAT3 | No catalyst | 0 | 6.8 | 2.1 | 250.2 | 0.32 |
| CAT4 | $NH_4OH$ | 0.05 | 9.6 | 1.6 | 365.3 | 0.33 |
| CAT5 | $NH_4OH$ | 0.30 | 13.0 | 1 | 375.1 | 0.35 |

The pH values were recorded right before hydrolysis reaction. The relative anatase crystallinity was calculated from the relative intensity of the diffraction peak of anatase (101) plane (reference: CAT5 sample dried at 100 °C).

tion reactions occur simultaneously when titanium tetraisopropoxide (TTIP) mixes with water [16,17]. The polycondensation reaction induces polymerization forming higher molecular weight products (nuclei and subsequently particles) [18,19]. These two reactions are sensitive to the reaction conditions, such as type and amount of solvent, water concentration, type and amount of catalysts, reaction temperature, mixing conditions, and so on. Thus, the photocatalytic activity and microstructure of the obtained titania powders depend strongly on the above reaction conditions. Song and co-workers [20–24] reported the effects of water concentration, calcination and hydrolysis temperatures, dopants, type and amount of catalyst, and alcohol solvents on microstructures of bimodally nanostructured porous titania powders. Ito et al. [14] found that the volume ratio of $H_2O$ to EtOH was a key factor influencing crystallinity and photocatalytic activity of $TiO_2$ particles prepared from the $H_2O$–EtOH mixed solution of $TiOSO_4$. Very recently, we have also reported the effects of water content and ultrasonic irradiation on the enhancement of photocatalytic activity of nanometer-sized $TiO_2$ powders prepared by the sol–gel method. It was found that ultrasonic irradiation obviously enhanced the photocatalytic activity of $TiO_2$ powders, for both cases where the solvent is pure water or where it is a mixed solution of EtOH/$H_2O$. This may be ascribed to the fact that ultrasonic irradiation enhances hydrolysis of titanium alkoxide and crystallization [8,9]. However, to the best of our knowledge, effects of $HNO_3$ and $NH_4OH$ catalysts added during hydrolysis on the photocatalytic activity and microstructures of titania powders prepared by hydrolysis of TTIP and under ultrasonic irradiation have not been reported.

In this study, highly photocatalytically active nanometer-sized $TiO_2$ photocatalysts with different phase compositions have been prepared by sol–gel process and ultrasonic treatment in an EtOH–$H_2O$ solution. The effects of the amount of $HNO_3$ and $NH_4OH$ catalysts on the microstructures and photocatalytic activity of bimodal mesoporous titania powders were investigated by X-ray diffraction (XRD), nitrogen adsorption, scanning electron micrograph (SEM), X-ray photoelectron spectroscopy (XPS), and photocatalytic oxidation of acetone. The scope of this study is to describe how different acid and basic catalysts influence the crystallinity and ultimately the photocatalytic activity of mesoporous titania.

## 2. Experimental

### 2.1. Preparation

All chemicals used in this study were reagent grade supplied from Aldrich and were used as received. Millipore water was used in all experiments.

Titanium tetraisopropoxide [$Ti(OC_3H_7)_4$, 97%] was used as a titanium source. To moderate its high reactivity, the TTIP was first diluted in anhydrous ethyl alcohol (molar ratio of ethyl alcohol/TTIP = 3) before reaction with water. In this study, $HNO_3$ and $NH_4OH$ were used as hydrolysis catalysts. The molar ratio of catalyst/TTIP was varied in the range of 0 to 0.5. Table 1 summarizes the preparation conditions of different samples of titania powders. Different amounts of the hydrolysis catalysts in different samples were mixed with an equivalent amount of water (molar ratio of water/TTIP = 60). The hydrolysis was conducted at room temperature by adding the ethanol solution to the aqueous solution of various catalyst concentrations with vigorous stirring for 1 h. The slurry products containing white titanium hydroxide precipitates were then irradiated with ultrasound in an ultrasonic cleaning bath (Bransonic ultrasonic cleaner, Model 3210E DTH, 47 kHz, 120 W, USA) for 2 h, followed by aging in a closed beaker at room temperature for 24 h in order to further hydrolyze the TTIP. After aging, these samples were heated at 100 °C for about 24 h in air to remove water and alcohol in the gels and then ground to fine powders to obtain xerogel samples. The xerogel samples were calcined at 400, 500, 600, and 700 °C in air for 1 h, respectively.

### 2.2. Characterization

The X-ray diffraction patterns obtained on a Philips MPD 18801 X-ray diffractometer using Cu-$K_\alpha$ radiation at a scan rate of 0.05° $2\theta$ $s^{-1}$ were used to determine the identity of any phase present and their crystallite size. The accelerating voltage and applied current used were 35 kV and 20 mA, respectively. The phase content of a sample can be calculated

from the integrated intensities of anatase (101), rutile (110), and brookite (121) peaks. If a sample contains only anatase and rutile, the mass fraction of rutile ($W_R$) can be calculated from [25]

$$W_R = \frac{A_R}{0.886A_A + A_R}, \tag{1}$$

where $A_A$ and $A_R$ represent the integrated intensities of the anatase (101) and rutile (110) peaks, respectively. If brookite is also present in a sample, similar relations can be derived [25],

$$W_A = \frac{K_A A_A}{K_A A_A + A_R + K_B A_B}, \tag{2a}$$

$$W_R = \frac{A_R}{K_A A_A + A_R + K_B A_B}, \tag{2b}$$

$$W_B = \frac{K_B A_B}{K_A A_A + A_R + K_B A_B}, \tag{2c}$$

where $W_A$ and $W_B$ represent the mass fractions of anatase and brookite, respectively. $A_B$ is the integrated intensity of the brookite (121) peak, and $K_A$ and $K_B$ are two coefficients and their values are 0.886 and 2.721, respectively. With Eq. (2), the phase contents in any $TiO_2$ samples can be calculated. The average crystallite sizes of anatase, rutile, and brookite were determined according to the Scherrer equation using the fwhm data of each phase [25].

Usually, the anatase phase of titania is the main product in hydrolytic sol–gel synthesis of nanocrystalline titania. However, brookite is also typically present in synthesis products. Brookite can be detected by the appearance of its (121) peak in powder X-ray diffraction patterns at $2\theta = 30.8°$. However, in some previous studies, the existence of a significant brookite phase was overlooked [26,27]. Even if the intensity of the brookite (121) peak is very low compared to the anatase (101) peak, the amount of brookite may be considerable [25,28].

Particle sizes and shapes were observed using scanning electron microscopy (Japan). The Brunauer–Emmett–Teller (BET) surface area ($S_{BET}$) of the powders was obtained with nitrogen adsorption in a Micromeritics ASAP 2010 nitrogen adsorption apparatus. For xerogel samples dried at 100 °C, the samples were degassed at 100 °C prior to actual measurements. However, for xerogel samples calcined at higher temperatures (from 400 to 700 °C), the degassing temperature was 180 °C. The BET surface area was determined by the multipoint BET method using the adsorption data in the relative pressure ($P/P_0$) range of 0.05–0.25. The pore-size distribution, based on the desorption branch of the isotherm, was estimated using the method developed by Barret, Joyner, and Halender (BJH), assuming a cylindrical pore modal [29–31].

### 2.3. Photocatalytic activity measurement

Acetone ($CH_3COCH_3$) is a common chemical used extensively in a variety of industrial and domestic applications. Therefore, we chose it as a model contaminant. Photocatalytic oxidation of acetone is based on the following reaction [32,33]:

$$CH_3COCH_3 + 4O_2 \rightarrow 3CO_2 + 3H_2O. \tag{3}$$

The photocatalytic activity experiments on the prepared $TiO_2$ powders and Degussa P-25 (P25) for the oxidation of acetone in air were performed at ambient temperature using a 7000-ml reactor. The photocatalyst samples for oxidation measurement were prepared by coating onto the inner surfaces of petri dishes (7.0 cm in diameter) the $TiO_2$ powders left behind from the evaporation of the water in a $TiO_2$ aqueous suspension. The weight of the photocatalyst used for each experiment was kept at 0.3 g, and the samples were cooled to room temperature before measurement. After sample-coated dishes were placed in the reactor, a small amount of acetone was injected into the reactor. The reactor was connected to a $CaCl_2$-containing dryer used for controlling the initial humidity in the reactor. The analysis of acetone, carbon dioxide, and water vapor concentration in the reactor was conducted on line with a Photoacoustic IR Multigas Monitor (INNOVA Air Tech Instruments Model 1312) [9,21]. The acetone vapor was allowed to reach adsorption equilibrium with the catalyst in the reactor prior to UV light irradiation. The initial concentration of acetone after adsorption equilibrium was about 400 ppm, which remained constant until a 15-W 365-nm UV lamp (Cole-Parmer Instrument Co.) in the reactor was switched on. Integrated UV intensity in the range 310–400 nm striking the coatings was measured with a UV radiometer (UVX, UVP Inc., CA) and was $540 \pm 10$ μW/cm$^2$, while the peak wavelength of UV light was 365 nm. The initial concentration of water vapor was $1.20 \pm 0.01$ vol%, and the initial temperature was $25 \pm 1$ °C. During the photocatalytic reaction, a near 3:1 ratio of carbon dioxide products to acetone destroyed was observed, and the acetone concentration decreased steadily with UV illumination time. Each set of experiments was followed for 60 min.

The photocatalytic activity of the coatings can be quantitatively evaluated by comparing the apparent reaction rate constants. The photocatalytic degradation generally follows a Langmuir–Hinshelwood mechanism [1,2,33,34] with the rate $r$ being proportional to the coverage $\theta$.

$$r = k\theta = kKc/(1 + Kc), \tag{4}$$

where $k$ is the true rate constant which includes various parameters such as the mass of catalyst and the intensity of light, and $K$ is the adsorption constant. Since the initial concentration is low ($c_0 = 400$ ppm $= 4.29 \times 10^{-3}$ mol/L), the term $Kc$ in the denominator can be neglected with respect to unity and the rate becomes, apparently, first order,

$$r = -\mathrm{d}c/\mathrm{d}t = kKc = k_a c, \tag{5}$$

where $k_a$ is the apparent rate constant of pseudo-first order. The integral form $c = f(t)$ of the rate equation is

$$\ln c_0/c = k_a t. \tag{6}$$

The photocatalytic behavior of Degussa P-25 was also measured as a reference to compare with the synthesized catalysts. The measurements were repeated for each catalytic system, and the experimental error was found to be within ±3%.

## 3. Results and discussion

### 3.1. Phase structures

Figs. 1a–c show the XRD patterns of the CAT1, CAT3, and CAT5 $TiO_2$ powders calcined at different temperatures, respectively. Table 1 shows the effects of $HNO_3$ and $NH_4OH$ catalysts added during hydrolysis on relative anatase crystallinity of $TiO_2$ xerogel dried at 100 °C. Table 2 shows the effects of $HNO_3$ and $NH_4OH$ catalysts on phase structure and average crystalline size of $TiO_2$ xerogel powders calcined at different temperatures. Apparently, the type of catalysts added during hydrolysis influences the phase structures and crystallization of the xerogel powders at 100 °C. Xerogel powders made with $HNO_3$ (CAT1) and without catalyst (CAT3) at 100 °C produce the same XRD patterns and both contain the anatase and brookite phases. There is, however, a small difference in crystallinity between CAT1 and CAT3. Table 1 and Fig. 1 show that CAT1 is slightly more crystalline, as indicated by the relative crystallinity of anatase. Interestingly, when $NH_4OH$ is used as the hydrolysis catalyst, the xerogel powders of CAT5 dried at 100 °C contain only the anatase phase, and the relative crystallinity of anatase also decreases. These results are different from those observed by Song and Pratsinis [23] and Terabe et al. [35], who found only anatase in the powders prepared with HCl catalyst. They claimed that the anatase phase is more stable than the amorphous phase in acidic solutions. So et al. [36] studied the crystalline phase of titania they prepared using a sol–gel method followed by a peptizing treatment with $HNO_3$. They found that both anatase and rutile could be formed even at room temperature. It was speculated that $H^+$ ions added would rearrange the amorphous aggregates to form the crystalline phases [36]. These discrepancies in the literature may be ascribed to different preparation methods and hydrolysis conditions. In general, the greater the relative crystallinity, the better the crystallization becomes. It can be concluded from Table 1 and Fig. 1 that $HNO_3$ enhances the crystallization of anatase while $NH_4OH$ reduces it under our experimental conditions.

Figs. 1a–c and Table 3 also show that the types of hydrolysis catalyst obviously influence the phase composition and transformation temperature of anatase to rutile. For CAT1, with increasing calcination temperature (from 100 to 600 °C), the peak intensities of anatase increase and the width of the (101) plane diffraction peak of anatase ($2\theta = 25.4°$) becomes narrower; the crystallization of titania is also enhanced. At 600 °C, brookite disappears and rutile is formed, and the $TiO_2$ powders contain only anatase and rutile. For CAT3, a trace amount of rutile appears at 600 °C, and the $TiO_2$ powders contain all three phases of anatase, brookite and rutile. At 700 °C, rutile is the main phase and brookite is gone. Table 3 shows that with increasing calcination temperature, the brookite contents in

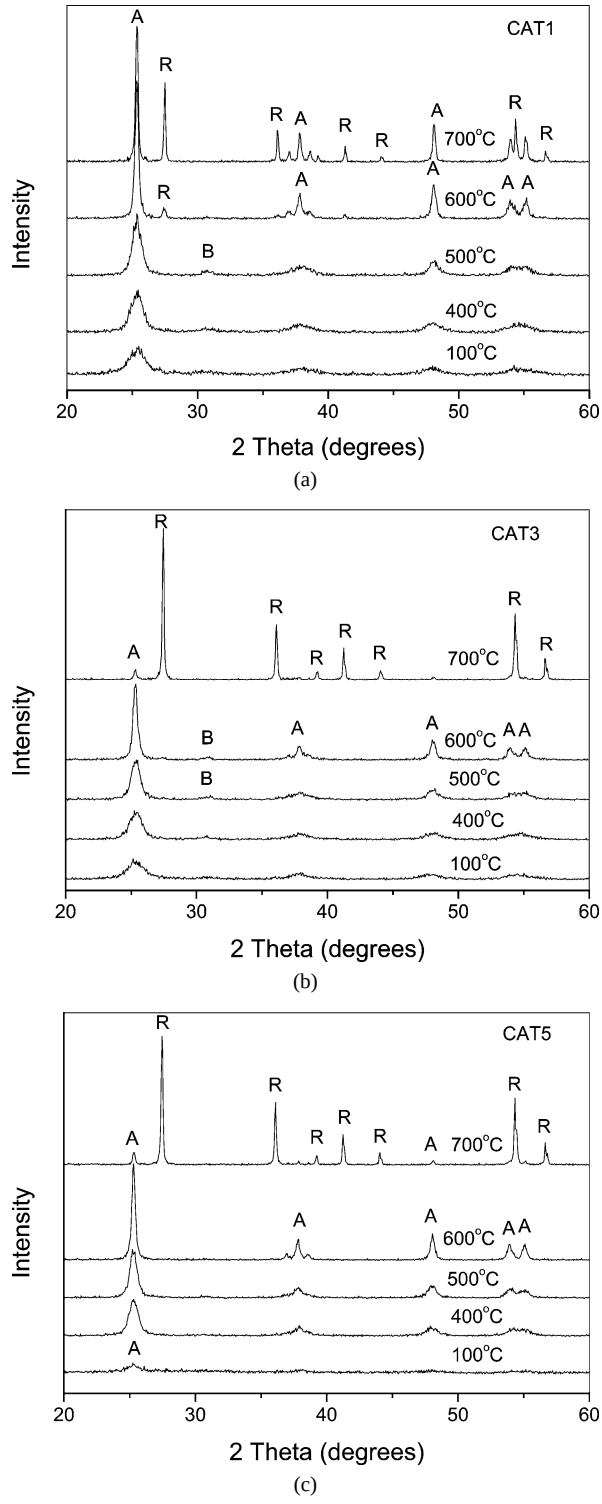


Fig. 1. XRD patterns of the (a) CAT1, (b) CAT3, and (c) CAT5 powders (Table 1) as a function of calcination temperature. The peaks marked A, R, and B represent the anatase, rutile, and brookite phase, respectively.

Table 2
Effects of catalysts and calcination temperatures on phase structures and average crystalline size (nm) of $TiO_2$

| $R_{EtOH}$ | 100 °C 24 h | 400 °C 1 h | 500 °C 1 h | 600 °C 1 h | 700 °C 1 h |
|---|---|---|---|---|---|
| CAT1 ($HNO_3$) | A: 5.7 nm, B: 3.6 nm | A: 6.4 nm, B: 5.9 nm | A: 10.6 nm, B: 7.7 nm | A: 28.3 nm, R: 25.7 nm | A: 40.3 nm, R: 62.2 nm |
| CAT3 | A: 5.1 nm, B: 4.0 nm | A: 6.8 nm, B: 5.7 nm | A: 10.4 nm, B: 7.3 nm | A: 23.0 nm, B: 9.5 nm, R: 52.2 nm | A: 39.3 nm, R: 62.2 nm |
| CAT5 ($NH_4OH$) | A: 4.9 nm | A: 9.3 nm | A: 12.4 nm | A: 28.3 nm | A: 36.6 nm, R: 55.8 nm |

A, B, and R denote anatase, brookite, and rutile, respectively. Average crystalline size of $TiO_2$ was determined by XRD using the Scherrer equation.

Table 3
Effects of $HNO_3$ and $NH_4OH$ catalysts on phase content of $TiO_2$

| $R_{EtOH}$ | 100 °C 24 h | 400 °C 1 h | 500 °C 1 h | 600 °C 1 h | 700 °C 1 h |
|---|---|---|---|---|---|
| CAT1 ($HNO_3$) | A: 65.2, B 34.8 | A: 73.5, B 26.5 | A: 76.5, B 23.5 | A: 92.2, R: 7.8 | A: 60.2, R: 39.8 |
| CAT3 | A: 68.6, B 31.4 | A: 70.0, B 30.0 | A: 75.0, B 25.0 | A: 84.0, B 14.0, R 2 | A: 6.4, R 93.6 |
| CAT5 ($NH_4OH$) | A: 100 | A: 100 | A: 100 | A: 100 | A: 8.4, R 91.6 |

A, B, and R denote anatase, brookite, and rutile, respectively.

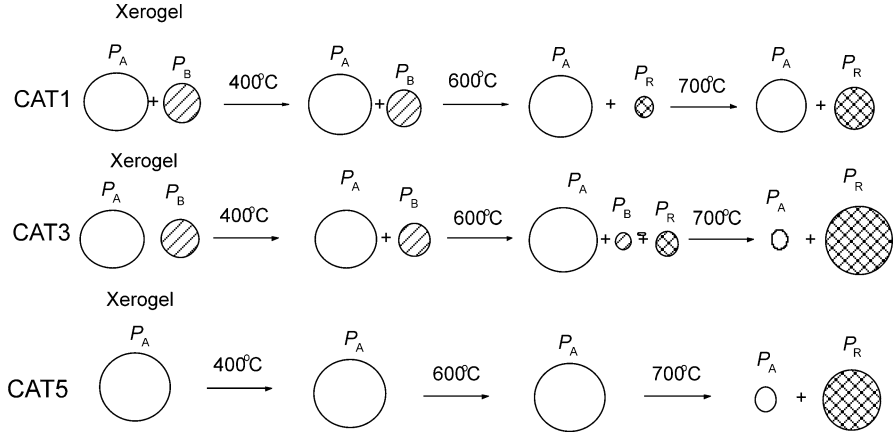


Fig. 2. Schematic model of the phase transformations in the samples calcined at different temperatures. $P_A$, anatase; $P_B$, brookite; $P_R$, rutile. The concentrations of different phases are roughly illustrated by the area size of the circles.

CAT1 and CAT3 diminish and finally reach zero at 600 and 700 °C. For CAT5, there is no trace of brookite, and the phase transformation of anatase to rutile occurs at 700 °C. It is also interesting to note from Table 3 that $HNO_3$ catalyst enhances the growth of brookite, while $NH_4OH$ retards such growth as well as the phase transformation from anatase to rutile. The detailed mechanism is not clear. The different processes of phase transformation occurring in the three samples are illustrated in Fig. 2. Table 2 and Fig. 3 also show that with increasing calcination temperature, the average crystallite size of anatase increases. From 500 to 700 °C, there is a steep increase of anatase crystal size due to phase transformation from anatase to rutile as a result of the heat provided to accelerate grain growth [8–10].

### *3.2. BET surface areas and pore structure*

Fig. 3 also shows the specific surface areas of the CAT1, CAT3, and CAT5 powders calcined at different temperatures. All powders show a monotonic decrease of the specific surface area with increasing calcination temperature due to the crystallite growth and phase transformation. It is interesting to observe that the CAT5 powder shows higher surface area than the CAT3 and CAT1 powders at 100 °C, but exhibits smaller surface area at 400 °C or higher. This can be ascribed to the fact that, at 100 °C, the CAT3 and CAT1 powders had better crystallization and larger crystallite size. At 400 °C or higher, the crystallite size of the CAT5 powders exceeds those of CAT3 and CAT1.

To compare the pore structure of the as-prepared xerogel powders at 100 °C, their nitrogen adsorption and desorption isotherms are presented in Fig. 4 for the CAT1, CAT3, and CAT5 powders. The isotherms corresponding to the CAT1 and CAT3 powders are of type IV (BDDT classification) [30] and have two hysteresis loops, indicating bimodal pore size distributions in the mesoporous region. The shapes of the two hysteresis loops are different from each other. At low relative pressure between 0.4 and 0.7, the hysteresis loops are of type H2, which can be observed in the pores with narrow necks and wider bodies (ink-bottle pores) [30]. However, at high relative pressure between 0.8 and 1.0, the shape of the hysteresis loops is of type H3 associated with aggregates of platelike particles giving rise to slitlike pores [30]. For $NH_4OH$ catalyst, the isotherm of the CAT5 powders at 100 °C is a combination of types I and IV

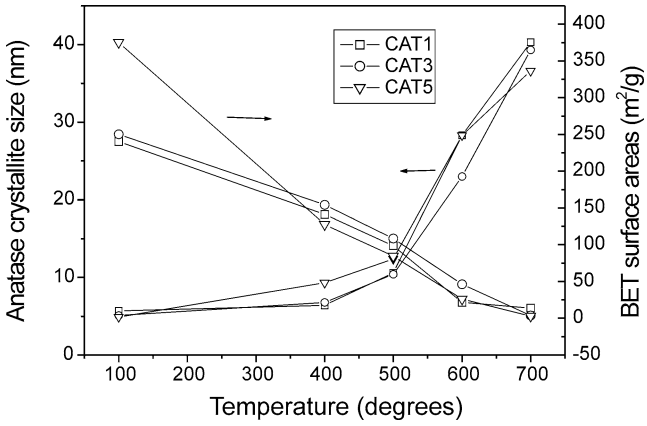


Fig. 3. Anatase crystallite size and BET surface areas of the CAT1, CAT2, and CAT3 powders as a function of calcination temperature.

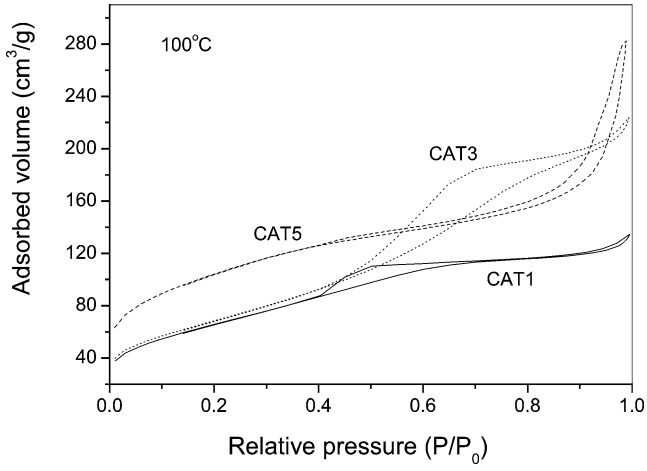


Fig. 4. Nitrogen adsorption and desorption isotherms of the (a) CAT1, (b) CAT3, and (c) CAT5 $TiO_2$ xerogel powders at 100 °C.

(BDDT classification) with two very distinct regions: At low relative pressure, the isotherm exhibits high adsorption, indicating that the powder contains micropores (type I). However, at high relative pressures between 0.8 and 1.0, the curve exhibits a hysteresis loop indicating the presence of mesopores (type IV). The shape of the hysteresis loop is of type H3, associated with plate-like particles giving rise to narrow slit-shaped pores [30,31].

Fig. 5 shows the pore-size distributions of the CAT1, CAT3, and CAT5 titania xerogel powders at 100 °C. The CAT3 powders dried at 100 °C show bimodal pore-size distributions consisting of fine intraaggregated pores with a maximum pore diameters of 4.7 nm and larger interaggregated pores with a maximum pore diameter of 42 nm. According to Kumar et al. [37], a bimodal pore-size distribution is due to hard aggregates in the powders. There are two types of pores present in the bimodal pore size distribution. One is the finer intraaggregated pore (represented by the hysteresis loop in the lower $P/P_0$ range) and the other is the larger interaggregated pore (hysteresis loop in the higher $P/P_0$ range).

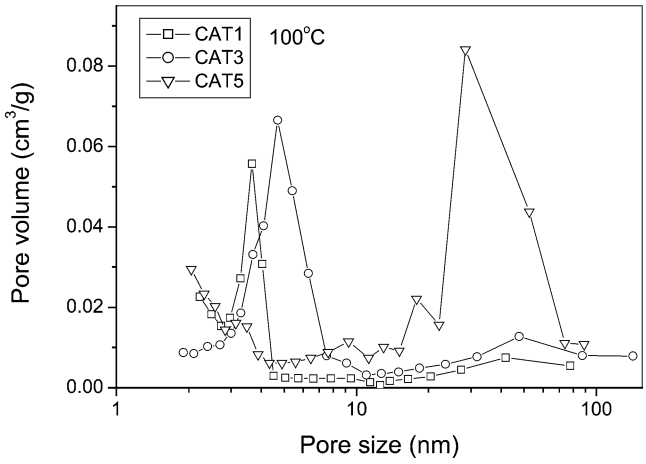


Fig. 5. Pore-size distribution curves of the (a) CAT1, (b) CAT3, and (c) CAT5 $TiO_2$ xerogel powders dried at 100 °C.

It is interesting to note that the maximum pore sizes of the intraaggregated and interaggregated pores in CAT1 powders are less than those in CAT3 powders. Also, the pore volumes of the intraaggregated and interaggregated pores in CAT1 powders are less than those in CAT3 powders. The difference in the pore-size distributions and pore volumes between powders prepared with $HNO_3$ as catalyst and without catalyst can be explained by the influence of the peptization step [23,38] on the dispersion of primary particles in the sol. For the powders prepared under excess $HNO_3$, protons ($H^+$) from $HNO_3$ are adsorbed on the surface of the primary particles. As most particles carry a positive charge, they repel each other to form a stable sol with a minimum degree of aggregation. On the other hand, the sol consisting of powders prepared at low $HNO_3$ concentrations or without catalyst contains nonuniform, highly aggregated clusters of primary particles. Since the powders prepared with excess $HNO_3$ have fewer aggregates and the primary particles in the powders are packed more uniformly, the maximum pore diameter and pore volume become smaller.

The dried powders prepared using $NH_4OH$ catalyst exhibit bimodal pore-size distributions, consisting of fine intraaggregated micropores and larger interaggregated mesopores. It is also observed from Fig. 5 that the maximum pore diameters of the intraaggregated pores and the interaggregated pores decrease with the addition of $NH_4OH$ catalyst. This may again be ascribed to the fact that hydroxyl ions ($OH^-$) from $NH_4OH$ are adsorbed on the surface of the primary particles. These particles carrying the same charge would also repel each other. When the solvents were evaporated at 100 °C, the primary particles within the powders are packed more uniformly and closely, thus the maximum pore diameter in the intraaggregated and the interaggregated become smaller.

Figs. 6a–c show the pore-size distributions of CAT1, CAT3, and CAT5 powders calcined at different temperatures, respectively. For the CAT1 and CAT3 powders, the pores show bimodal distributions consisting of the intraag-

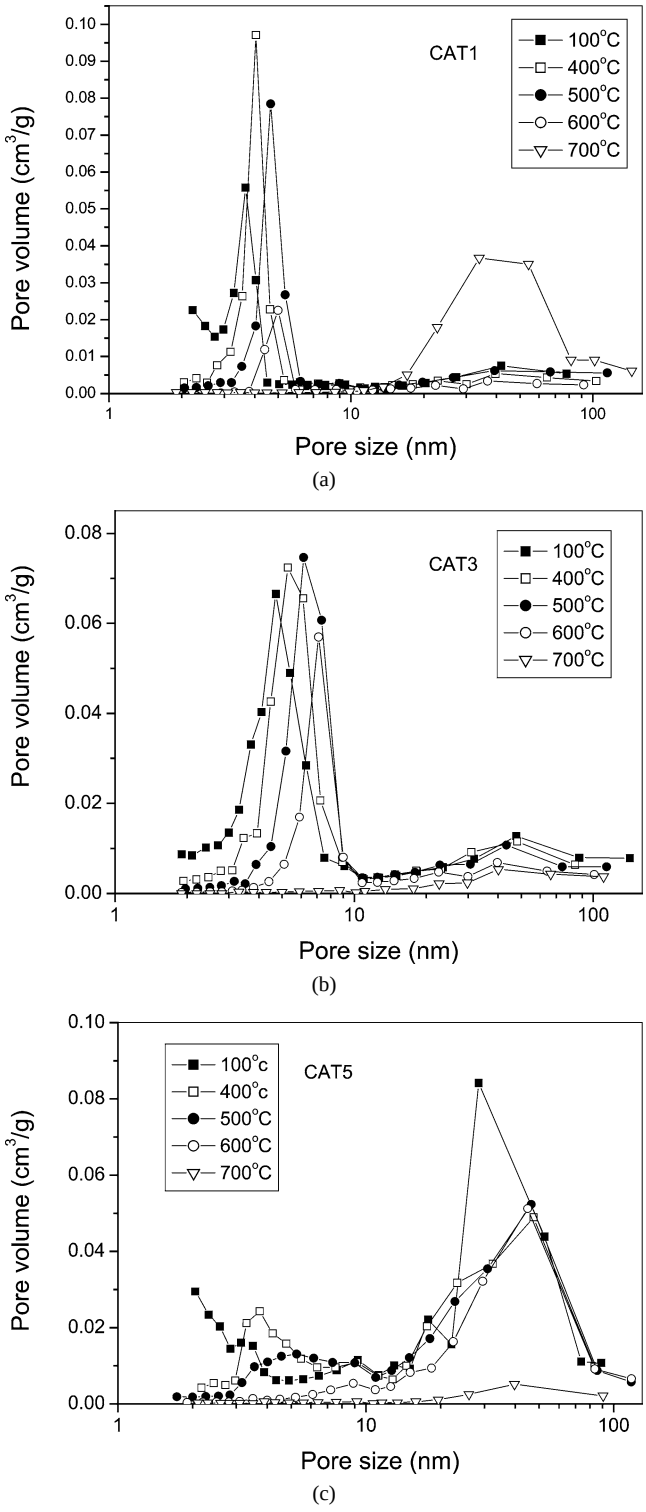


Fig. 6. Pore-size distribution curves of the (a) CAT1, (b) CAT3, and (c) CAT5 powders as a function of calcination temperatures.

gregated and interaggregated pores from 100 to 600 °C. At 700 °C, the pores exhibit monomodal distribution of the interaggregated pores due to the collapse of intraaggregated pores. The maximum pore size of the intraaggregated pores in the CAT1 and CAT3 powder calcined at 400 °C lies in

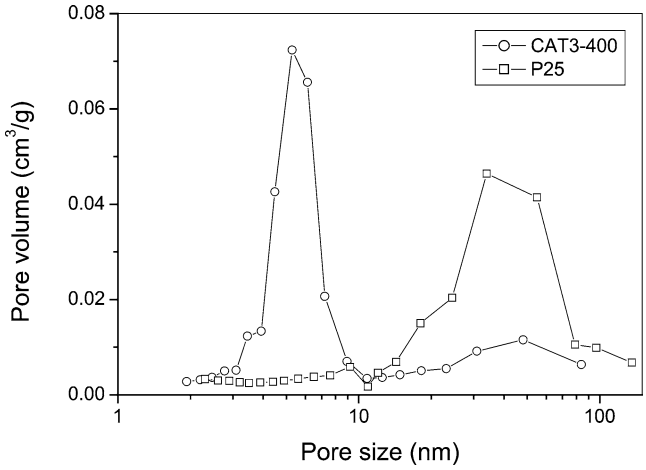


Fig. 7. Comparison of the pore-size distribution curves of the CAT3 powder calcined at 400 °C and Degussa P-25 powder.

4.0 and 5.3 nm, respectively. However, when the powder is calcined 500 and 600 °C, the maximum pore size of the intraaggregated pores shifts into the larger mesoporous region, indicating the growth of pores. This is caused by the growth of anatase crystallites. The bimodal pore-size distributions are also observed in the CAT5 powders (shown in Fig. 6c). The maximum pore volume of the intraaggregated pores in the powder dried at 100 °C lies in the microporous region. However, when the powder is calcined from 400 to 600 °C, the maximum pore size of the intraaggregated pores shifts into the mesoporous region (3.7–9.0 nm), indicating the growth of pores. This is caused by the crystallization and growth of anatase crystallites. At 700 °C, the pores also exhibit monomodal distribution of the interaggregated pores for CAT5 powders. Therefore, it can be inferred that, at 700 °C, hydrolysis catalyst has no influence on the pore-size distributions.

Fig. 7 shows the comparison of pore-size distributions of the CAT3 powders calcined at 400 °C and Degussa P-25 titania powders prepared by flame hydrolysis of $TiCl_4$. The P25 powder has smaller specific surface area (53.2 $m^2/g$) than the CAT3 powder calcined at 400 °C (154.1 $m^2/g$). It also shows a totally different pore-size distribution. The pore structure of the P25 powder is monomodal with a maximum pore diameter at 34 nm. However, the pore-size distribution of the CAT3 powder is bimodal and shows two maximum values at 5.3 and 47.0 nm.

Fig. 8 shows scanning electron micrographs of the CAT1 (a, b), CAT3 (c, d), and CAT5 (e, f) powders calcined at 500 °C. The CAT1 powders show a dense structure with fewer aggregates, resulting in the decrease in the pore volume of the large interaggregated pores in Fig. 6a. The CAT3 powders prepared without catalyst show highly aggregated and nonuniform structure, resulting in the higher pore volume of the large interaggregated pores in Fig. 6b. On the other hand, the CAT5 powders show microstructures of uniform, compact secondary particles with smaller size.

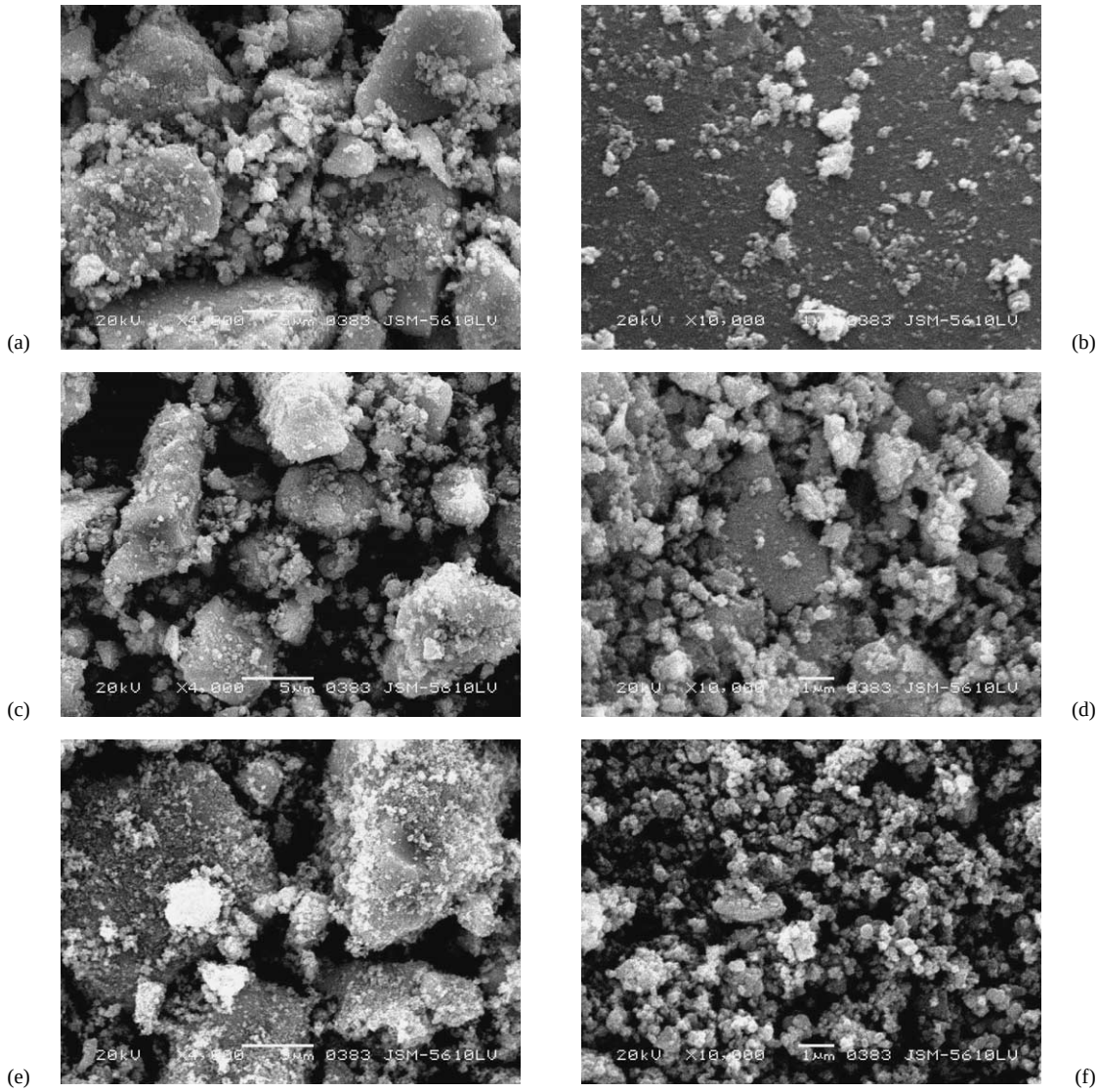


Fig. 8. SEM micrographs of (a, b) CAT1, (c, d) CAT3, and (e, f) CAT5 powders calcined at 500 °C.

Hence, the pore volume of the larger interaggregated pores is the greatest (as shown in Fig. 6c).

### 3.3. Photocatalytic activity

Fig. 9 shows the dependence of the apparent rate constants ($k$, $\text{min}^{-1}$) of the CAT1, CAT3, and CAT5 powders on calcination temperature. For the CAT3 powder dried at 100 °C, it showed good photocatalytic activity. Its $k$ reached $3.75 \times 10^{-3}$. This is ascribed to the formation of anatase and brookite at 100 °C (as shown in Fig. 1b) and high specific surface areas (as shown in Fig. 3). With increasing calcination temperature, $k$ obviously increases. This is due to the fact that $TiO_2$ shows better crystallization (as shown in Fig. 1b). At 400 °C, $k$ reaches its highest value of $5.51 \times 10^{-3}$, obviously higher than that of P25 (as shown in Fig. 10). The $k$ was determined to be $4.19 \times 10^{-3}$ for Degussa P-25, which is well known to have good photocatalytic activity [1,20]. The superior activity shown by CAT3 cal-

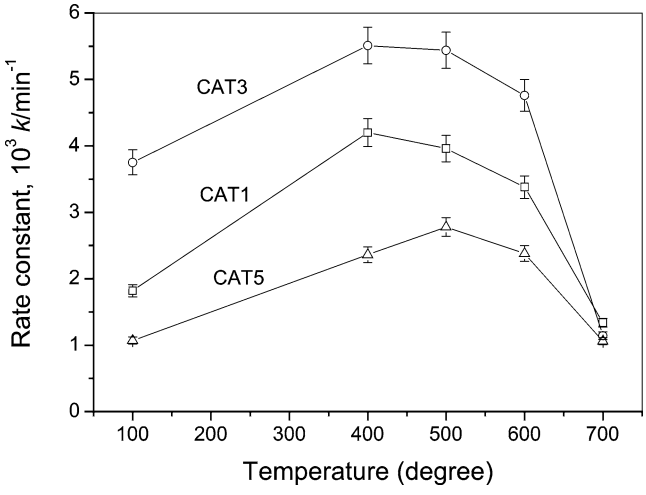


Fig. 9. The dependence of the apparent rate constant ($k$, $\text{min}^{-1}$) of the CAT1, CAT3, and CAT5 powders on calcination temperature.

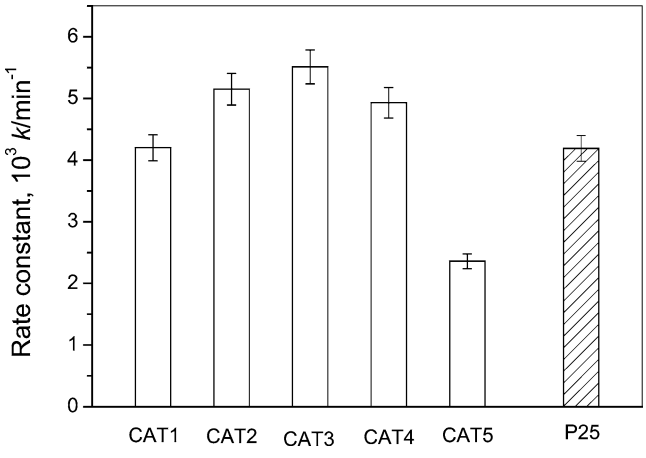


Fig. 10. Comparison of the apparent rate constants of P25 and the CAT1–5 powders calcined at 400 °C for 1 h.

cined at 400 °C may be ascribed to the fact that it has larger specific surface area, smaller crystallite size, and higher purity. The specific surface area and crystallite size of P25 are about 53.2 $m^2/g$ and 30 nm, respectively. Our XPS results also show that P25 contains a small amount of Cl element (about 0.5 at.%). At 600 °C, though the specific surface area (46.3 $m^2/g$) of the CAT3 powder is slightly less than that of P25, the photocatalytic activity of the CAT3 powders exceeded that of P25. This may be attributed to the former having bimodal mesoporous structures, which is more beneficial in enhancing the adsorption and desorption of reactants and products, respectively. At 700 °C, the $k$ values for CAT1, CAT3, and CAT5 decrease significantly and reach almost the same magnitude. The former is probably due to the phase transformation from anatase to rutile, disappearance of bimodal mesoporous structures, crystalline growth, and drastic decrease in specific surface areas. The latter is due to all samples having almost the same microstructure, specifically, pore distribution, specific surface areas.

Fig. 10 also shows that with an addition of $HNO_3$ or $NH_4OH$ catalyst during hydrolysis, the $k$ decreases at 400 °C. When the amount of the added $HNO_3$ and $NH_4OH$ catalyst is low and the molar ratio of $HNO_3$ or $NH_4OH$ to $H_2O$ is less than 0.05, the photocatalytic activity of the prepared $TiO_2$ powders decreases slightly but still exceeds that of Degussa P-25. With increasing concentration of $HNO_3$, the photocatalytic activity of the prepared titania obviously decreases. This is probably due to the decrease in pore volume (the pore volumes of CAT1 and CAT3 samples at 400 °C are 0.164 and 0.233, respectively). When the concentration of $NH_4OH$ is high, the photocatalytic activity of the prepared titania at 400 °C drops significantly. This can be explained by the presence of a single anatase crystalline phase in the sample. It is known that a composite of two phases is beneficial for suppressing the recombination of photogenerated electrons and holes and thus enhances photocatalytic activity [8,9].

## 4. Conclusions

1. The phase structures, texture, and photocatalytic activity of titania powders prepared by hydrolysis of titanium tetraisopropoxide under ultrasonic irradiation are strongly influenced by the presence of acidic or basic catalysts. When $HNO_3$ is used as a catalyst, the crystallization of anatase phase and growth of brookite phase are slightly enhanced. In contrast, the $NH_4OH$ not only retards the phase transformation of the $TiO_2$ powders from amorphous to anatase and from anatase to rutile but also suppresses the growth of brookite phase.

2. At 100 °C, the maximum intraaggregated and interaggregated pore diameter decreases with increasing $HNO_3$ or $NH_4OH$ concentration. From 400 to 600 °C, the calcined $TiO_2$ powders show bimodal pore-size distributions in the mesoporous region: one is intraaggregated pores with maximum pore diameters of ca. 4–9 nm and the other is interaggregated pores with maximum pore diameters of ca. 35–50 nm. At 700 °C, the pore-size distributions of all samples exhibit monomodal distribution of the interaggregated pores due to the collapse of the intraaggregated pores.

3. The photocatalytic activity of the $TiO_2$ powders prepared by this method and calcined at 400 °C is higher than that of Degussa P-25 when the molar ratio of $HNO_3$ or $NH_4OH$ to $H_2O$ is less than 0.05.

## Acknowledgments

The work was partially supported by a grant from the National Natural Science Foundation of China and Research Grants Council of the Hong Kong Special Administrative Region, China (Project No. N_CUHK433/00). This work was also financially supported by The Excellent Young Teachers Program of MOE, P.R.C., Foundation for University Key Teachers of the Ministry of Education, and the National Natural Science Foundation of China (50272049, 50072016).

## References

[1] M.R. Hoffmann, S.T. Martin, W. Choi, D.W. Bahnemann, Chem. Rev. 95 (1995) 69.
[2] A. Fujishima, T.N. Rao, D.A. Tryk, J. Photochem. Photobiol. C 1 (2000) 1.
[3] A.L. Linsebigler, G. Lu, J.T. Yates Jr., Chem. Rev. 95 (1995) 735.
[4] H. Tada, M. Yamamoto, S. Ito, Langmuir 15 (1999) 3699.
[5] C. Hu, Y.Z. Wang, H.X. Tang, Appl. Catal. B 30 (2001) 277.
[6] C. Hu, Y.Z. Wang, H.X. Tang, Chemosphere 41 (2000) 1205.
[7] M. Gopal, W.J.M. Chan, L.C. DeJonghe, J. Mater. Sci. 32 (1997) 6001.
[8] J.C. Yu, J.G. Yu, W.K. Ho, L.Z. Zhang, Chem. Commun. (2001) 1942.
[9] J.C. Yu, J.G. Yu, W.K. Ho, J.C. Zhao, J. Photochem. Photobiol. A 148 (2002) 263.
[10] J.G. Yu, J.C. Yu, W.K. Ho, Z.T. Jiang, New J. Chem. 26 (2002) 607.
[11] M.A. Fox, M.T. Dulay, Chem. Rev. 93 (1993) 341.
[12] J. Ovenstone, J. Mater. Sci. 36 (2001) 1325.

[13] K.N.P. Kumer, K. Keizer, A.J. Burggraaf, T. Okubo, H. Nagamoto, S. Morooka, Nature 358 (1992) 48.
[14] S. Ito, S. Inoue, H. Kawada, M. Hara, M. Iwasaki, H. Tada, J. Colloid Interface Sci. 216 (1999) 59.
[15] G.W. Koebrugge, L. Winnubst, A.J. Burggraaf, J. Mater. Chem. 3 (1993) 1095.
[16] K. Terabe, K. Kato, H. Miyazaki, S. Yamaguchi, A. Imai, Y. Iguchi, J. Mater. Sci. 29 (1994) 1617.
[17] B.E. Yoldas, J. Mater. Sci. 21 (1986) 1087.
[18] H.K. Bowen, Mater. Sci. Eng. 65 (1986) 1574.
[19] J.S. Chappell, L.J. Procopio, J.D. Birchall, J. Mater. Sci. Lett. 9 (1990) 1329.
[20] K.C. Song, S.E. Pratsinis, J. Mater. Res. 15 (2000) 2322.
[21] J. Kim, K.C. Song, S.E. Pratsinis, J. Nanoparticle Res. 2 (2000) 419.
[22] J. Kim, K.C. Song, S. Foncillas, S.E. Pratsinis, J. Eur. Ceram. Soc. 21 (2001) 2863.
[23] K.C. Song, S.E. Pratsinis, J. Am. Ceram. Soc. 84 (2001) 92.
[24] K.C. Song, S.E. Pratsinis, J. Colloid Interface Sci. 231 (2000) 289.
[25] H. Zhang, J.F. Banfield, J. Phys. Chem. B 104 (2000) 3481.
[26] K.N.P. Kumar, K. Keizer, A.J. Burggraaf, J. Mater. Chem. 3 (1993) 1141.
[27] Y.S. Lin, C.H. Chang, R. Gopalan, Ind. Eng. Chem. Res. 33 (1994) 860.
[28] J.C. Yu, J.G. Yu, W.K. Ho, Z.T. Jiang, L.Z. Zhang, Chem. Mater. 14 (2002) 3808.
[29] E.P. Barrett, L.G. Joyner, P.H. Halenda, J. Am. Chem. Soc. 73 (1951) 373.
[30] K.S.W. Sing, D.H. Everett, R.A.W. Haul, L. Moscou, R.A. Pierotti, J. Rouquerol, T. Siemieniewska, Pure Appl. Chem. 57 (1985) 603.
[31] S.J. Gregg, K.S.W. Sing, Adsorption, Surface Area and Porosity, Academic Press, London, 1982.
[32] J. Lin, J.C. Yu, D. Lo, S.K. Lam, J. Catal. 183 (1999) 368.
[33] J.C. Yu, J.G. Yu, J.C. Zhao, Appl. Catal. B 36 (2002) 31.
[34] A. Fernandez, G. Lassaletta, V.M. Jimenez, A. Justo, A.R. Gonzalez-Elipe, J.M. Herrmann, H. Tahiri, Y. Ait-Ichou, Appl. Catal. B 7 (1995) 49.
[35] K. Terabe, K. Kato, H. Miyazaki, S. Yamaguchi, A. Imai, Y. Iguchi, J. Mater. Sci. 29 (1994) 1617.
[36] W.W. So, S.B. Park, S.J. Moon, J. Mater. Sci. Lett. 17 (1998) 1219.
[37] K.N.P. Kumar, J. Kumar, K. Keizer, J. Am. Ceram. Soc. 77 (1994) 1396.
[38] B.L. Bischoff, M.A. Anderson, Chem. Mater. 7 (1995) 1772.